Modification of the Mechanical Properties of Core-Shell Liquid Gallium Nanoparticles by Thermal Oxidation at Low Temperature

Sergio Catalán-Gómez,* Andrés Redondo-Cubero, Miguel Morales, María de la Mata, Sergio I. Molina, Francisco J. Palomares, Alberto Carnicero, Jose L. Pau, and Luis Vázquez*

Gallium nanoparticles (Ga NPs) are attracting increasing attention because of their appealing physical-chemical properties. In particular, their mechanical properties play a key role in the implementation of these core-shell structures on certain applications, such as soft and stretchable electronics. Thus, efforts are being addressed to modulate them mainly by chemical means. In contrast, this study investigates how the mechanical properties of the outer gallium thin oxide shell change when its thickness is increased through a thermal oxidation strategy. Specifically, as-deposited Ga NPs, as well as those subjected to thermal oxidation at 300 °C for three different times, are studied by performing single-particle indentations by atomic force microscopy over a wide range of NP radius. This analysis helps to confirm that the Reissner's thin-shell model for small deformations within the elastic regime is obeyed. From these data, the dependence of the shell stiffness and the Young's modulus of the gallium oxide on the thermal treatment is obtained. It is found that the shell stiffness increases with the annealing time, even by a factor of 50 under prolonged thermal oxidation, while the gallium oxide Young's modulus, close to 30 GPa, does not change significantly.

1. Introduction

Nanoparticles (NPs) are attracting increasing attention from the scientific community due to their multiple applications.[1–3] In particular, those that present a liquid core surrounded by a solid shell, named liquid metal nanoparticles (LMNPs), are characterized by having low melting points, which makes their liquid state accessible to practical applications in various fields of chemical and physical sciences.[4] LMNPs exhibit unique properties such as fluidic flexibility in shape simultaneously with standard metallic properties, including high thermal and electrical conductivities, high density, as well as the ability to respond to electric and magnetic fields.[5] Furthermore, LMNPs present low toxicity, biocompatible behavior, photothermal conversion ability, are prone to be chemically functionalized, and have cancer suppressor capabilities.[6] These

S. Catalán-Gómez, A. Redondo-Cubero, J. L. Pau
Grupo de Electrónica y Semiconductores
Departamento de Física Aplicada
Universidad Autónoma de Madrid
Madrid E-28049, Spain
E-mail: sergio.catalan.gomez@upm.es

S. Catalán-Gómez
Institute for Optoelectronics Systems and Microtechnology
ISOM
Universidad Politécnica de Madrid
Madrid E-28040, Spain

The ORCID identification number(s) for the author(s) of this article can be found under https://doi.org/10.1002/ppsc.202100141.

M. Morales
Instituto Galego de Física de Altas Enerxías (IGFAE)
Universidade de Santiago de Compostela
Galicia E-15782, Spain

M. de la Mata, S. I. Molina
Departamento de Ciencia de los Materiales
Ingeniería Metalúrgica y Química Inorgánica
Universidad de Cádiz
Puerto Real E-11510, Spain

F. J. Palomares, L. Vázquez
Instituto de Ciencia de Materiales de Madrid
CSIC
Madrid E-28049, Spain
E-mail: lvb@icmm.csic.es

A. Carnicero
Institute for Research in Technology
Universidad Pontificia Comillas
Madrid E-28015, Spain

properties turn them into appealing candidates for bio-related field applications, including cancer therapy, medical imaging, biosensing, and pathogen treatment.[7–6] In addition, liquid metals possess the ability to be patterned into non-spherical shapes using different methods to form highly conductive and durable interconnects with direct application in microfluidics and soft, flexible, and stretchable electronics.[9–13] For the latter application, it becomes essential to control the mechanical properties of these core-shell NPs.

The deformation limits of conductors formed by liquid metal are basically determined by the mechanical properties of the encasing shell material, which has a critical role. It is typically constituted by a native oxide that preserves the NP liquid shape integrity while acting as a "skin", which under rupture makes the system conductive.[14,15] In this sense, it is necessary to assess the mechanical properties of the shell. This can be made experimentally either by analyzing an ensemble of NPs[16] or by studying single NPs.[17,18] In the single-particle case, atomic force microscopy (AFM) is being increasingly employed since it offers a high spatial resolution together with the capability to use small forces, in the range from pN to µN.[18] In this case, some compression studies have been performed with simultaneous optical control, which allows to correlating the geometrical deformation of the particle with increasing applied forces.

Among the wide range of LMNPs and their alloys,[4] gallium (Ga) based LMNPs have stood out over other materials,[19,20] mainly because of their metallic properties since their localized surface plasmon resonances (collective oscillations of electrons) can be tuned from the ultraviolet to the infrared range of the electromagnetic spectrum.[21] Ga NPs can be grown by a simple, fast, and cost-effective manner by thermal evaporation at low substrate temperature, which makes them compatible with many conductive and insulating substrates.[22–24] During deposition on flat surfaces, liquid Ga forms truncated, quasi hemispherical NPs due to the surface tension induced relaxation. Ga NPs merge during the growth due to coalescence or coarsening processes, typically ascribed to the Ostwald ripening mechanism,[25] resulting in wide size distributions with large NPs surrounded by smaller ones.[26] When exposed to air, after the growth, a very thin native oxide (Ga_xO_y) is formed around the liquid core preserving it from the environment. This shell thickness is assumed to be self-limited (≈3 nm) by the attenuation of the oxygen diffusion.[27] As the NP size decreases to the nanoscale, its mechanical properties become dominated by those of the oxide shell, which has important implications for several applications.[28] For this reason, recent efforts aim at controlling the core-shell properties mainly through tuning the shell thickness. This has been attempted mainly by chemical modification of the oxide layer,[28] either by thiolation[29] or with phosphonic acids.[30]

In this work, we report on the results obtained on Ga NPs by using a new strategy, specifically by thermal oxidation.[31] This procedure, in contrast to those mentioned above, does not imply any chemical modification on the shell. Moreover, it preserves the shell composition except for a more homogeneous stoichiometry upon prolonged annealing.[26] This strategy does not appreciably change the NP radius but, importantly, it allows to tune the shell thickness up to values close to thrice those attained by the chemical routes. This larger thickness range

improves the assessment of the dependence of the mechanical properties on this parameter. Thus, here we study the mechanical properties of Ga NPs by AFM indentations of a wide range size of NPs with a high statistical significance (more than 800 NPs were analyzed). More specifically, we have studied these properties not only for the as-deposited Ga NPs, but also for NPs thermally oxidized at 300 °C for different times, namely, 15, 400, and 1200 min, which leads to increasing shell thickness. This study addresses the influence of thermal oxidation on the mechanical properties of the NPs, in particular, the gallium oxide Young's modulus and the shell stiffness. As explained below, we have limited this study to gentle force loads to ensure that only the mechanical properties of the outer shell are sampled. This study is possible thanks to the low force values that can be applied with the AFM. In future work, we will address the processes involved when high forces, even leading to the shell rupture, are applied. Finally, it should be noted that the scarce works that have already addressed the study of the mechanical properties of metallic liquid core/solid shell systems are restricted to eutectic Ga-In alloys.[28,32,33]

2. Theory of NP Deformation

In this report, we address the mechanical characterization of the Ga_xO_y shell of the as-deposited as well as of the annealed Ga NPs. This study implies that neither buckling nor rupture of the shell take place. Under these conditions, the theory of elasticity predicts a linear elastic response for a spherical shell indented by a point load, as it is the present case, when the ratio between the shell thickness, h, and the NP radius, R, is close to 0.1,[17] and the indentation displacement, δ, is on the order of h.[34,35] In this initial regime, Reissner's model states that:

$$F = K_{shell}\delta = \frac{4Eh^2\delta}{R\sqrt{3(1-v^2)}} \quad (1)$$

where F is the applied load, and v and E are the Poisson ratio and the Young's modulus of the Ga_xO_y, respectively. From this relationship, the shell stiffness, K_{shell}, is:

$$K_{shell} = \frac{4Eh^2}{R\sqrt{3(1-v^2)}} = m/R \quad (2)$$

In this case, m includes all the parameters of the right side of Equation (2) that multiply $1/R$. In m are included v, h, and E. Thus, whereas h may change, both v and E, are, in principle (see below), constant as they are material properties. Therefore, whereas E is constant K_{shell} depends on morphological parameters such as R and h. Certain corrections on this linear relationship have been reported for the indentation of a spherical particle placed on a rigid substrate.[36] However, they do not apply to this case due to the hemispherical shape of the NPs that leads to a large contact area between the NPs and the surface of the silicon (Si) substrate. Finally, it should be noted that the reported range of application of this model extends to h/R ratios up to 0.17.[28] This is the criterion followed in this study.

**ADVANCED
SCIENCE NEWS**
www.advancedsciencenews.com

Particle
& Particle Systems Characterization
www.particle-journal.com

Figure 1a shows a representative distance-force curve taken by AFM on a Ga NP. The solid line corresponds to the reference one obtained on the hard sapphire surface used for calibration
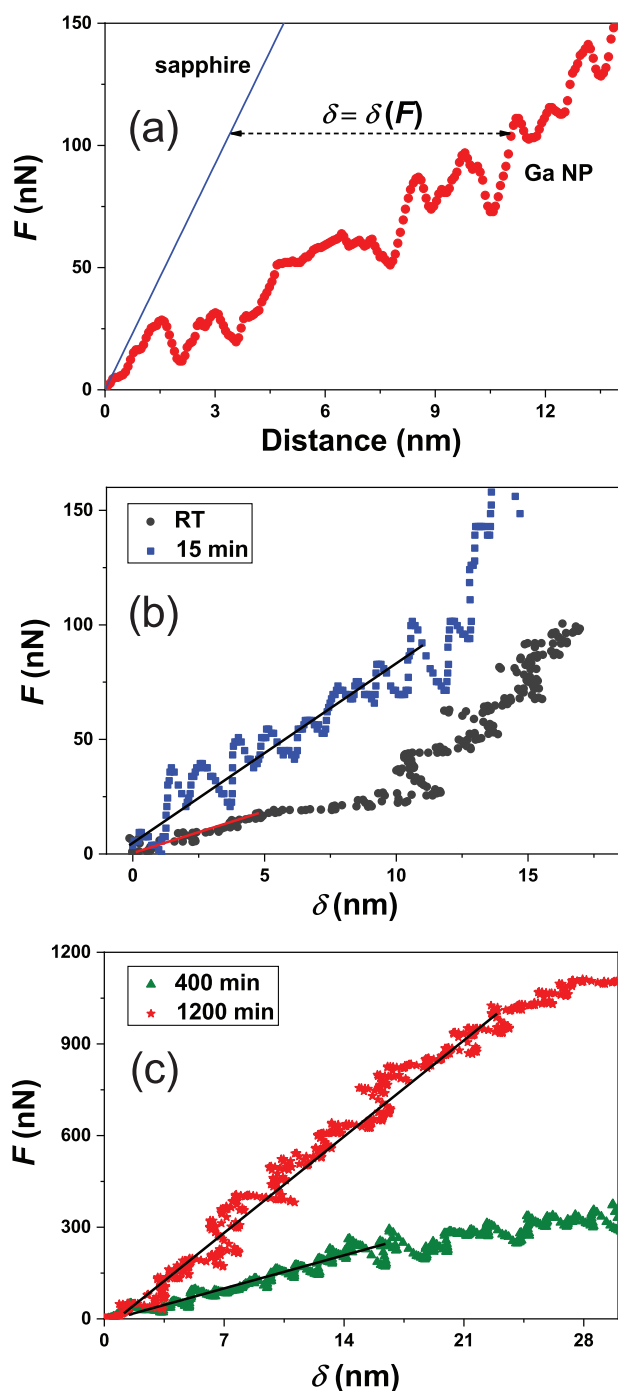

Figure 1. a) Representative force curve obtained on a Ga NP annealed for 15 min, together with the corresponding calibration curve taken on sapphire reference substrate. For each applied force, F, the corresponding displacement, δ, value is obtained as indicated. Typical F versus δ curves obtained for the as-deposited (RT) at b) 15 min and c) 400 and 1200 min annealed Ga NPs. The corresponding linear regimes are indicated by the solid lines. Note that δ range increases with the annealing time in agreement with the corresponding h value increment.

purposes. From these curves, the indentation displacement, δ, can be obtained for each applied force. From Equation (1), the shell stiffness, K_{shell}, can be obtained.

From these data, the corresponding F versus δ plots can be obtained for each NP of each system (Figure 1b, c). Despite the fluctuations or oscillations in the curves, a clear initial linear regime can be observed for all cases. The longer the oxidation time the larger the δ range of this regime, in concordance with the increment in h with the annealing time as explained below. Similar oscillations have also been reported in related systems.[35]

3. Ga NPs Size Distribution

As can be seen in Equation (2), the Reissner's model predicts a dependence of K_{shell} on the inverse of the NP radius. Thus, in order to assess the validity of this relationship over a wide range of NP sizes, we produced two different sets of Ga NPs depositions on Si (see experimental). **Figure 2** shows typical SEM images of both sets, denoted as samples A (Figure 2a) and B (Figure 2b), including their size distribution histograms (Figure 2c). Notice that the particle size spans almost one order of magnitude.

4. Results and Discussion

In order to proceed with the indentation experiments, once a stable AFM imaging in the dynamic mode is achieved, the NPs are selected, and on their apex, the corresponding force spectroscopy experiments are performed (see Experimental section). Afterwards, the analyzed NPs are checked by AFM imaging to be sure that the data are obtained within the elastic regime (without NP rupture). Following the procedure depicted in Figure 1, the corresponding (R, K_{shell}) data were obtained. **Figure 3** displays the obtained data for the four different samples (as-deposited sample (RT) and 15, 400, and 1200 min annealed samples).

Despite the relative data scattering (note the large number of analyzed NPs), it is evident that for all systems $K_{shell} \propto 1/R$, in accordance with Reissner's model, indicated by the dashed lines. One remarkable conclusion from these results is the shell stiffness increment up to 50 times upon thermal oxidation at 300 °C for 1200 min. Furthermore, it increases as the oxidation time does.

We tested the reliability of the measurements by proving various cantilevers with different spring constant values (k_{tip}). In fact, the cantilever had to be carefully chosen to avoid artifacts as shown in Figure S1, Supporting Information. K_{shell} versus R data pair values obtained with cantilevers with different stiffness (k_{tip}) for the sample annealed at 300 °C for 15 min are shown (Figure S1a, Supporting Information). The data obtained with different cantilevers overlap for the range of R studied. In contrast, for the case of the sample oxidized during 1200 min (Figure S1b, Supporting Information) the use of a soft cantilever not only leads to smaller K_{shell} values but also to the loss of the Reissner's dependence K_{shell} on $1/R$, which indicates that a stiffer tip should be used. These facts were already reported

ADVANCED
SCIENCE NEWS
www.advancedsciencenews.com

Particle
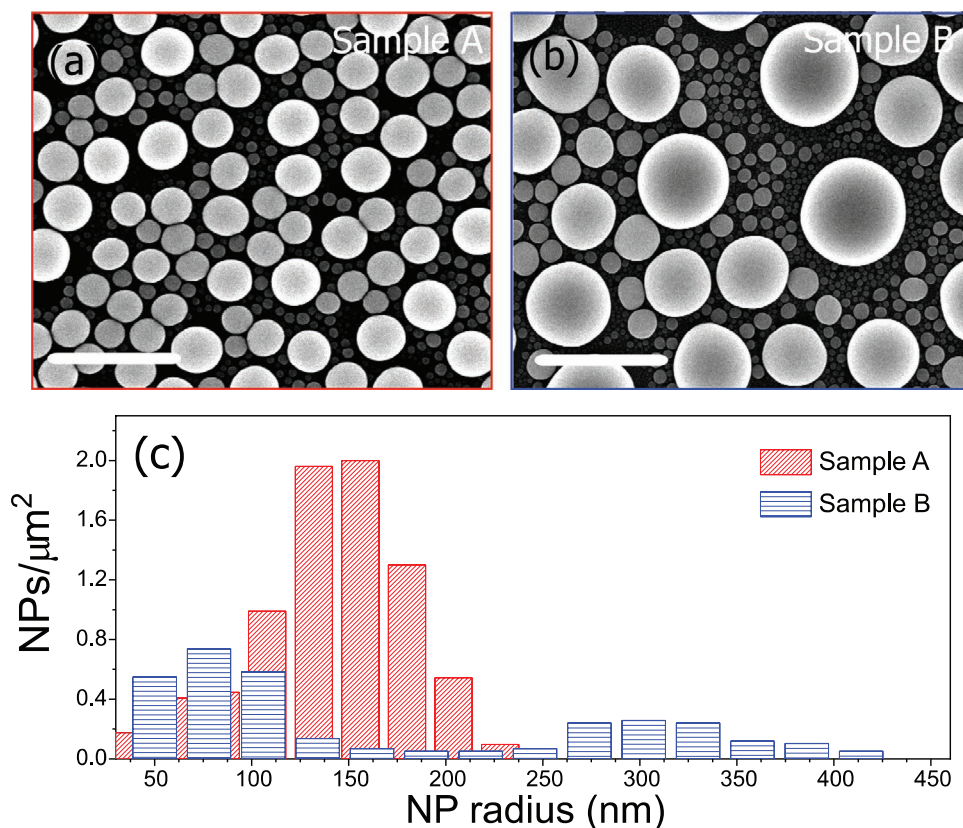& Particle Systems Characterization
www.particle-journal.com

Figure 2. a,b) Top view SEM images of both sets of Ga NPs deposited on Si substrates. Scale bar represents 1 μm. c) Corresponding size distribution histograms.

for hollow thin-shell polymer microspheres,[35] and confirmed here. Consequently, we have only considered for each system those data obtained with cantilevers for which a clear Reissner's dependence was observed.

The observed data scattering is likely due to multiple reasons. Thus, the force measurements may not take place exactly on the very apex of the hemisphere, leading to deviations or even instabilities.[35] Moreover, differences could also arise from changes in the tip status while measuring. However, the main source of data scattering might be related to the local changes in the shell thickness (h). As it can be seen in Equation (1) K_{shell} depends on the square of the thickness, that is, $K_{shell} \propto h^2$, having a strong influence on the final result. These local changes in the thickness of the oxide shell (Ga_xO_y) are evaluated by scanning transmission electron microscopy (STEM) analyses. **Figure 4** displays Z-contrast images of NPs of the as-deposited sample on Si substrate (Figure 4a) and after thermal oxidation at 300 °C for 1200 min (Figure 4b). The chemical contrast provided by the technique (brighter regions belong to heavier materials, that is, Ga_xO_y appears darker than Ga) allows the identification and measurement of the shell, whose composition has been further confirmed by electron energy-loss spectroscopy (EELS) (insets in Figure 4). Both samples (as-deposited and annealed during 1200 min) show the presence of NPs with Ga cores (brighter) surrounded by a thin Ga_xO_y shell layer (darker), evidencing thickness fluctuations within individual shells.

The issue of the shell thickness values becomes crucial to obtain the corresponding Young's modulus, E, of the Ga_xO_y shell from the relationship given in Equation (2). The m value is obtained by fitting m/R to the experimental data (see dashed lines in Figure 3a,b). Therefore,

$$E = \frac{m\sqrt{3(1-v^2)}}{4h^2} = 0.4117 m/h^2 \tag{3}$$

Where we have assumed a Poisson´s ratio, $v = 0.31$, for the Ga_xO_y shell.[28] In this relationship, the key role played by the h value on the E determination becomes evident. Our main approach to evaluate the h range for each NP system is based on X-ray photoelectron spectroscopy (XPS) measurements of the four samples that should provide a range for the h values. Due to the hemispherical geometry of the NPs, the values obtained by XPS are likely an overestimation of the actual ones because, depending on the escaping paths of the emitted electrons, they can emerge from the NPs along directions different from the local normal to the shell. We have employed both the Ga 2p and 3d levels due to their associated sampling depths, d, of 4 and ≈8 nm, respectively.[37,38] It should be explained that $d = 3\lambda$, being λ the inelastic mean free path that depends on the electron kinetic energy of each level. However, the main part, two-thirds, of the electrons emerges from depths close to λ (i.e., 1.4 and 2.8 nm, respectively for 2p and 3d levels).[39] These

**ADVANCED
SCIENCE NEWS**

www.advancedsciencenews.com

Particle
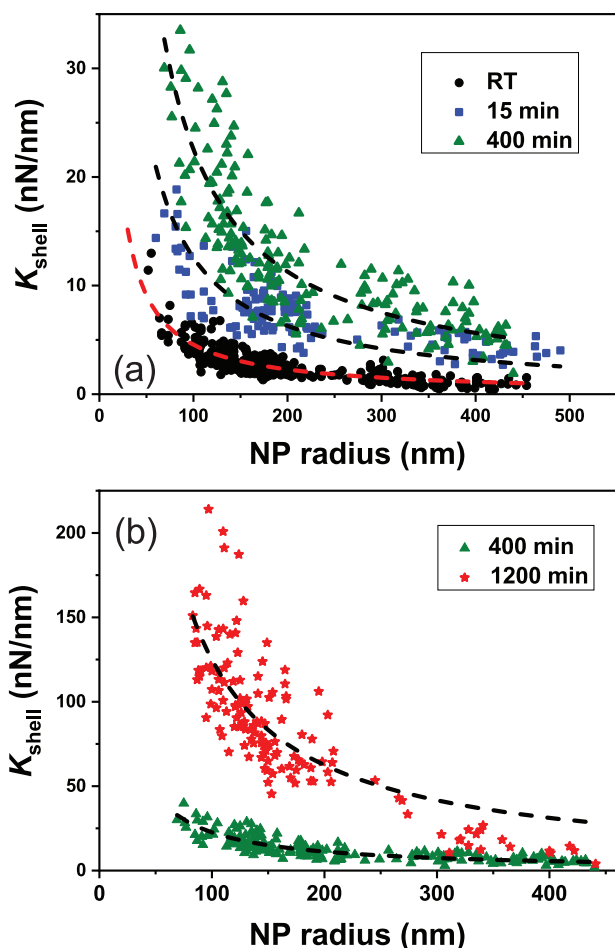& Particle Systems Characterization

www.particle-journal.com

Figure 3. Plots of K_{shell} versus NP radius for: a) As-deposited sample and those annealed at 300 °C for 15 and 400 min; b) samples annealed at 300 °C for 400 and 1200 min. Note the change in the scale of the y-axis. The dashed lines indicate the best fit with $1/R$ dependence. The values of the k_{tip} employed in each case are given in the Experimental Section.

Figure 4. Z-contrast STEM images of the a) as-deposited and the annealed sample at b) 300 °C for 1200 min where the liquid Ga core and the Ga_xO_y shell (arrows) can be identified. Insets display the oxygen (red-colored) EELS. c) XPS spectra of Ga 2p (left) and Ga 3d (right) levels for the samples oxidized at 300 °C during different times, including the as-deposited sample. Note, that the Ga 2p peak is superimposed on the tail of the larger Ga-O peak.

peaks are coming from metallic Ga below the shell, thus their attenuation will be due to the Ga_xO_y layer thickness.

Figure 4c shows the evolution of 2p and 3d photoelectron emission from the metallic Ga core of the NPs for increasing annealing times in the presence of oxygen. Clearly, both peak intensities decrease as the annealing time increases, that is, as the Ga-oxide shell thickness increases. For the as-deposited sample, there is a clear but slight 2p peak and a marked 3d peak. These features indicate that the Ga_xO_y thickness should lie mainly at values larger than 1.4 nm and much lower than 8 nm, being 2–3 nm a reasonable range for h, in agreement with the literature.[27,29] It must be noted that this result is also in agreement with the TEM measurements performed on the sample (see Figure 4a, where Ga NPs show a Ga_xO_y shell of 2–3 nm).

After 15 min of oxidation, a strong emission of the 3d peak is observed although its intensity has reduced by half, approximately. This indicates that h should be clearly smaller than 8 nm. In addition, a clear 2p emission is still present, which limits the shell thickness to a value close to, or higher than, 4 nm. Therefore, we can assume that the thickness lies in the
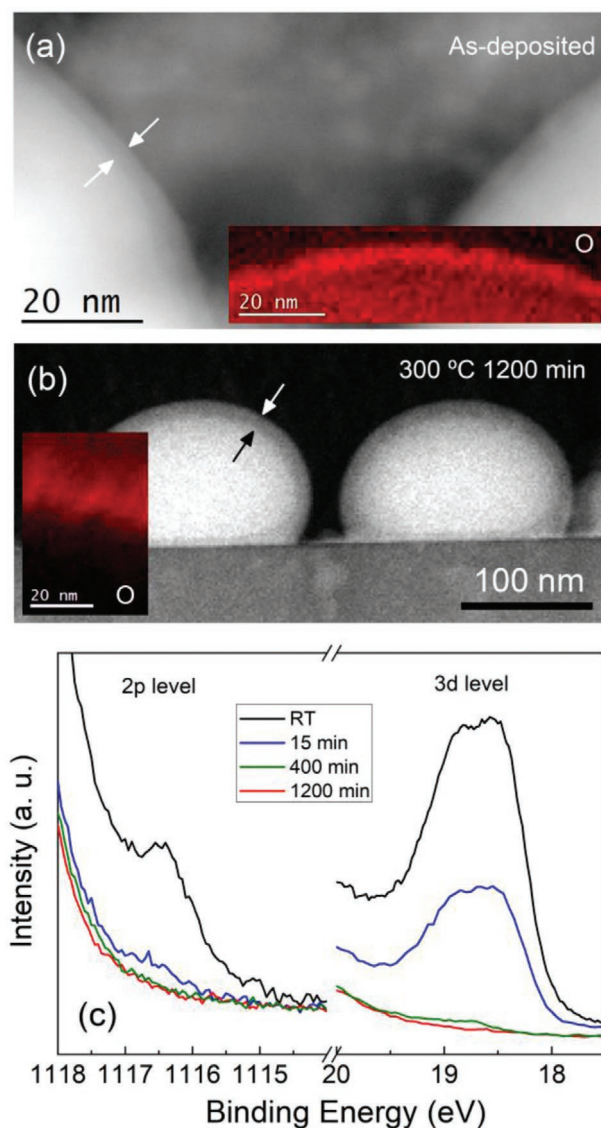
4–6 nm range. For the 400 min oxidized sample, the 3d peak has almost vanished, indicative of a thicker shell, which suggests an upper-value limit for h that should be close to 8 nm. Accordingly, we can assume a thickness in the 6–8 nm range. Finally, for the 1200 min oxidized sample, both peaks have disappeared, indicating that h is larger than 8 nm. The TEM measurements performed (including Z-contrast imaging and EELS) allow the estimation of the range of h values for this sample (Figure 4b), resulting in a shell thickness, h within the 9.5–13 nm range.

Figure 5a shows the E ranges for each sample (filled bars) estimated accounting for the corresponding estimated h ranges,

**ADVANCED
SCIENCE NEWS**

www.advancedsciencenews.com

Particle
& Particle Systems Characterization
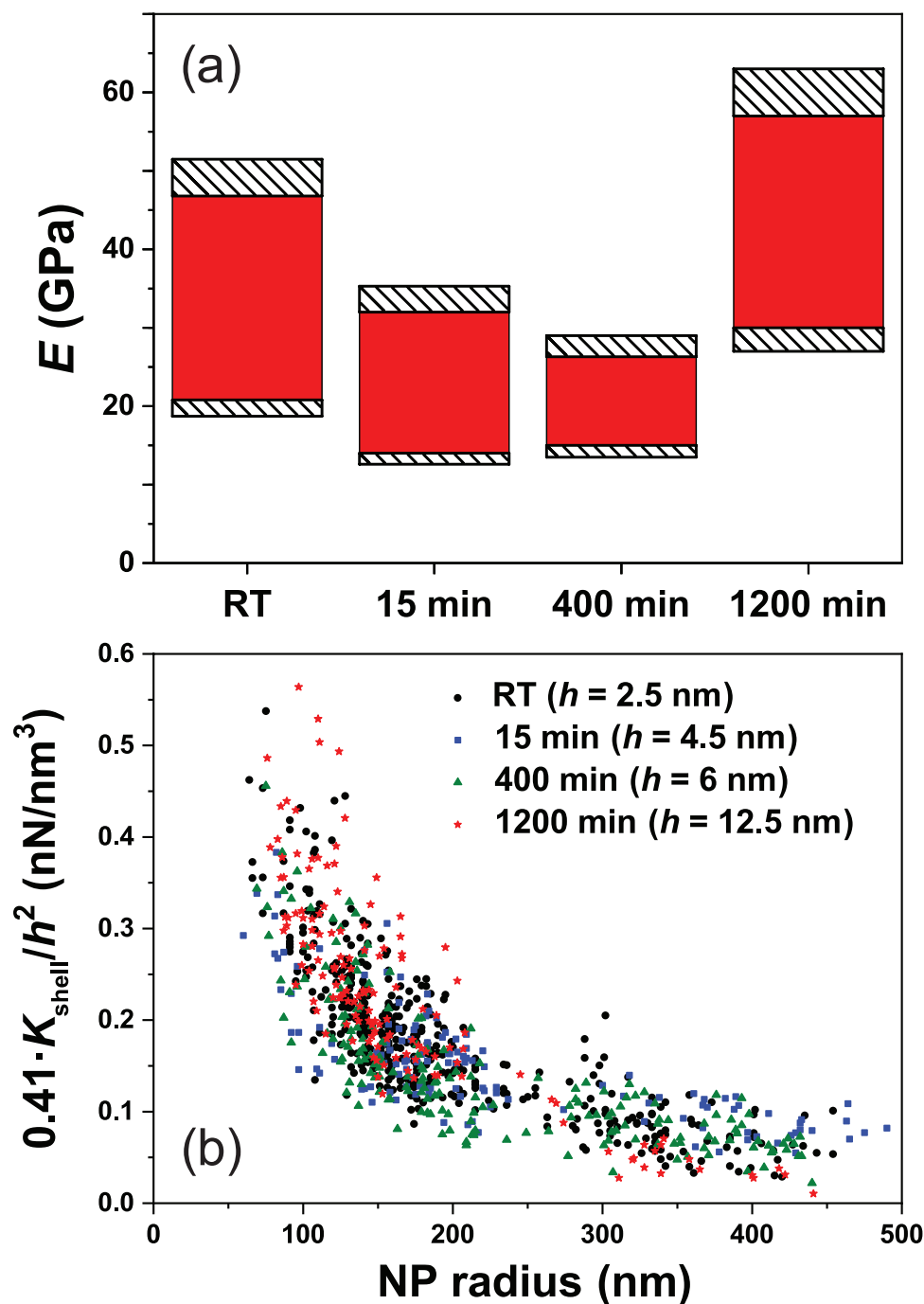
www.particle-journal.com

Figure 5. a) Range of Young's modulus (filled bars) for the four samples estimated by using h values extracted from TEM and XPS measurements for each sample. The dashed bars correspond to the 10% error associated with the cantilever spring constant value determination. b) Collapse of the K_{shell}/h^2 versus R data for all the samples (h values indicated in the plot legend).

along with the error associated with the cantilever spring constant (dashed pattern). It can be seen that the Young's modulus of the oxide does not change significantly with the oxidation time. Under this assumption, the plot of K_{shell}/h^2 versus R should collapse for all the samples (Figure 5b, where the specific h values used for such collapse are indicated). This collapse leads to $E \approx 30$ GPa, which is one order of magnitude lower

than that of an amorphous gallium oxide film.[40] As noted before,[28] this can be related to the fact that the shell, at this loading condition and due to its small thickness, behaves rather as a membrane than as a stiff shell. In this case, membrane-like behavior would be linked to the extreme shell thinness and a small capability to support bending moments that lead to an enhanced displacement upon loading.[41] Thus, the low E

**ADVANCED
SCIENCE NEWS**

www.advancedsciencenews.com

Particle
& Particle Systems Characterization

www.particle-journal.com

measured values and the marked shell thinness in our system suggest a membrane-like behavior. Similar behavior was found for thin (thickness smaller than 5 nm) gallium oxide shells.[28] However, for the sample annealed for 1200 min, the shell thickness is considerably larger and the membrane-like contribution should be lower, which would agree with its statistically larger measured E values.

The E value obtained here, even for the case of as-deposited conditions, is also one order of magnitude higher than that obtained on eutectic Ga-In NPs prepared by sonication from RT liquid metal. However, in that case not only the preparation method was different but also the characterization technique differed. In that case, a flat punch, up to 50 μm wide, was employed, thus sampling many NPs at the same time in contrast to our single-particle measurements. These differences may explain the different E values obtained. We should stress that we have employed different cantilevers with spring constants spanning from 3 Nm^{-1} up to 90 Nm^{-1}, and that only those data series where K_{shell} did change with the NP radius accordingly with the Reissner's model were considered.

Finally, it cannot be ruled out from Figure 5a that the longest oxidation time might induce a slight increase of the Young's modulus of the oxide layer. This would be consistent with our earlier findings through exhaustive XPS analysis.[26] Figure S2, Supporting Information, shows the XPS spectra of the 3d level of Ga for the as-deposited sample and the one annealed for 1200 min. The measured spectra have been fitted with the contributions of the so-called suboxides 1 and 2 (Ga$_2$O and GaO, respectively) and the oxide (Ga$_2$O$_3$) as previously performed.[26] Oxygen 2s broad peak fitting is also included. From the fittings, it is clear that the contribution of suboxides diminishes upon annealing resulting in a more homogeneous stoichiometry. Therefore, the formation of a more chemically stable oxide shell could possibly lead to a slight increase in E. In this sense, prolonged thermal oxidation could also cause a change of the oxide Poisson's ratio. However, given the dependence of E on ν (Equation (3)), it is not expected a marked change of E with ν.

5. Conclusions

The mechanical properties of the Ga$_x$O$_y$ shell of Ga NPs deposited on Si substrates by thermal evaporation, and subjected to thermal oxidation for different times, have been studied by means of AFM. Single-particle force curves have been obtained over a statistically relevant number of NPs and over a wide range of NP radius values. As low tip forces were applied, the elastic behavior of the oxide shell was addressed. This analysis allows us to verify that the Reissner´s thin-shell model for small deformations is obeyed provided that adequate cantilevers are employed. Thus, the shell stiffness (K_{shell}), extracted from the experimental data, was found to increase with the oxidation time, even by a factor of 50. From these data, as well as from those obtained by TEM and XPS, the corresponding shell thickness range value for each system was estimated, which allowed to conclude that, in contrast to the shell stiffness, the Ga$_x$O$_y$ Young's modulus (E), close to 30 GPa, does not change significantly with the thermal treatment.

6. Experimental Section

Nanoparticle Deposition and Thermal Annealing: The Ga NPs deposition procedure has been described elsewhere.[31] Briefly, they were deposited by Joule-effect thermal evaporation under a working pressure of 1.5×10^{-5} mbar on Si (100) substrates. Since the size of the NPs depends on the total amount of Ga (99.9999% purity) placed in the evaporation crucible, two samples were obtained with two different masses of Ga (340 and 410 mg) in order to study NPs with a wide range of sizes.

The thermal oxidation took place at atmospheric pressure in a horizontal quartz tube under a constant flow of 80 standard cubic centimeters of 99.999% pure O$_2$ to achieve the NPs oxidation. The temperature was fixed at 300 °C but different annealing times were employed (15, 400, and 1200 min). In Figure S3, Supporting Information, the NP size distribution obtained by SEM imaging of the as-prepared sample and after annealing at 300 °C for 1200 min are displayed. Within the resolution of the technique, there was not any appreciable change in the NP radius induced by the annealing process.

Scanning Electron Microscopy (SEM): The NPs were characterized with FEI XL30-SFEG equipment operating at 10 keV with a nominal lateral resolution of 4 nm and being the secondary electrons collected and analyzed with an Everhart–Thornley detector. NP size distributions were obtained from SEM images.

Transmission Electron Microscopy (TEM): The measurements were performed in scanning mode (STEM) under Z-contrast imaging conditions by using Jeol2010 and 60–300 kV Titan Cube FEI transmission electron microscope, provided with field-emission and X-FEG Schottky electron guns, respectively and both operated at 200 kV, achieving sub-nanometer spatial resolution. The system was equipped with a probe corrector and a Gatan DualEELS Spectrometer to carry out elemental atomic maps. Ga$_x$O$_y$ shell thickness range was estimated from this technique.

X-Ray Photoelectron Spectroscopy (XPS): XPS has also been used to estimate the thickness of the Ga$_x$O$_y$ shell, a key parameter to obtain the Young's modulus. The spectra were acquired in a UHV system with a base pressure of 10^{-10} mbar equipped with a hemispherical electron energy analyzer (SPECS Phoibos 150 spectrometer) and a 2D delay-line detector, using a monochromatic Al-Kα (1486.74 eV) X-ray source. (see more details in ref. [26]).

Atomic Force Microscopy (AFM): The measurements were done with Agilent 5500 Picoplus equipment operating with a closed-loop piezoelectric. First, AFM imaging in the dynamic mode was obtained. Once the consecutive images did not show any appreciable drift, force curves through indentation experiments were obtained on previously selected NPs. These curves were obtained at a speed close to 1 μm s^{-1} and were composed of at least 10 000 data points. The maximum force applied was controlled. The curves were analyzed by using homemade software specifically developed for force curve analysis. AFM imaging of the same area was performed after the force curve measurements to confirm that the NPs were neither indented nor broken, that is, that the force curves were obtained within the shell elastic regime. Different tips were employed (from Bruker) with a nominal radius of curvature of 8 nm. They differed in their spring constant from the 1–5 Nm^{-1} range up to close to 130 Nm^{-1} (see the discussion on their range of application in the explanation of Figure 3 and S1). Specifically, the RT sample was characterized with tips whose spring constants (k_{tip}) were 1.55, 1.8, and 3.1 Nm^{-1}. The 15 min oxidized sample with k_{tip} of 3.73, 4.2, and 31 Nm^{-1}. The 400 min annealed sample with tips of 73.8 and 83.4 Nm^{-1} and last, the 1200 min sample with tips whose k_{tip} were 74.1, 82, and 135 Nm^{-1}. All cantilevers were calibrated after the force curve measurements on sapphire surfaces in order to not damage them. For the softer tips, their spring constant values were obtained by the thermal tuning method.[42] For the stiffer cantilevers, with their dimensions, measured by SEM, and their resonance frequency and Q factor values, the corresponding spring constant values, with an error of 10%, were obtained using the Sader method.[43]

2100141 (7 of 8)

**ADVANCED
SCIENCE NEWS**

www.advancedsciencenews.com

Particle
& Particle Systems Characterization

www.particle-journal.com

Supporting Information

Acknowledgements

Conflict of Interest

The authors declare no conflict of interest.

Data Availability Statement

Research data are not shared.

Keywords

[1] V. V. Mody, R. Siwale, A. Singh, H. R. Mody, *J. Pharm. Bioallied Sci.* **2010**, *2*, 282.

[2] I. Khan, K. Saeed, I. Khan, *Arabian J. Chem.* **2019**, *12*, 908.

[3] J. Jeevanandam, A. Barhoum, Y. S. Chan, A. Dufresne, M. K. Danquah, *Beilstein J. Nanotechnol.* **2018**, *9*, 1050.

[4] T. Daeneke, K. Khoshmanesh, N. Mahmood, I. A. de Castro, D. Esrafilzadeh, S. J. Barrow, M. D. Dickey, K. Kalantar-zadeh, *Chem. Soc. Rev.* **2018**, *47*, 4073.

[5] J. Zhang, R. Guo, J. Liu, *J. Mater. Chem. B* **2016**, *4*, 5349.

[6] X. Sun, B. Yuan, H. Wang, L. Fan, M. Duan, X. Wang, R. Guo, J. Liu, *Adv. NanoBiomed Res.* **2021**, *1*, 2000086.

[7] H. Li, R. Qiao, T. P. Davis, S.-Y. Tang, *Biosensors* **2020**, *10*, 196.

[8] M. Zhang, X. Wang, Z. Huang, W. Rao, *Biosensors* **2020**, *10*, 170.

[9] K. Khoshmanesh, S.-Y. Tang, J. Y. Zhu, S. Schaefer, A. Mitchell, K. Kalantar-zadeh, M. D. Dickey, *Lab Chip* **2017**, *17*, 974.

[10] M. D. Dickey, *Adv. Mater.* **2017**, *29*, 1606425.

[11] S. Nagels, W. Deferme, *Materials* **2018**, *11*, 375.

[12] T. V. Neumann, B. Kara, Y. Sargolzaeiaval, S. Im, J. Ma, J. Yang, M. C. Ozturk, M. D. Dickey, *Micromachines* **2021**, *12*, 146.

[13] M. D. Dickey, *ACS Appl. Mater. Interfaces* **2014**, *6*, 18369.

[14] S. Liu, S. N. Reed, M. J. Higgins, M. S. Titus, R. Kramer-Bottiglio, *Nanoscale* **2019**, *11*, 17615.

[15] R. Zheng, Z. Peng, Y. Fu, Z. Deng, S. Liu, S. Xing, Y. Wu, J. Li, L. Liu, *Adv. Funct. Mater.* **2020**, *30*, 1910524.

[16] M. O'Sullivan, Z. Zhang, B. Vincent, *Langmuir* **2009**, *25*, 7962.

[17] B. Sarrazin, N. Tsapis, L. Mousnier, N. Taulier, W. Urbach, P. Guenoun, *Langmuir* **2016**, *32*, 4610.

[18] A. Fery, R. Weinkamer, *Polymer* **2007**, *48*, 7221.

[19] Y. Lin, J. Genzer, M. D. Dickey, *Adv. Sci.* **2020**, *7*, 2000192.

[20] M. de la Mata, S. Catalán-Gómez, F. Nucciarelli, J. L. Pau, S. I. Molina, *Small* **2019**, *15*, 1902920.

[21] S. Catalán-Gómez, C. Bran, M. Vázquez, L. Vázquez, J. L. Pau, A. Redondo-Cubero, *Sci. Rep.* **2020**, *10*, 4187.

[22] F. Nucciarelli, I. Bravo, S. Catalan-Gomez, L. Vázquez, E. Lorenzo, J. Pau, *Nanomaterials* **2017**, *7*, 172.

[23] M. Losurdo, A. Suvorova, S. Rubanov, K. Hingerl, A. S. Brown, *Nat. Mater.* **2016**, *15*, 995.

[24] S. Catalán-Gómez, C. Bran, N. Gordillo, F. Nucciarelli, M. Vázquez, J. L. Pau, A. Redondo-Cubero, *Nano Futures* **2018**, *2*, 041001.

[25] P. W. Woorhees, *J. Stat. Phys.* **1985**, *38*, 231.

[26] S. Catalán-Gómez, A. Redondo-Cubero, F. J. Palomares, L. Vázquez, E. Nogales, F. Nucciarelli, B. Méndez, N. Gordillo, J. L. Pau, *Nanotechnology* **2018**, *29*, 355707.

[27] J. M. Sanz, D. Ortiz, R. Alcaraz de la Osa, J. M. Saiz, F. González, A. S. Brown, M. Losurdo, H. O. Everitt, F. Moreno, *J. Phys. Chem. C* **2013**, *117*, 19606.

[28] N. J. Morris, Z. J. Farrell, C. E. Tabor, *Nanoscale* **2019**, *11*, 17308.

[29] Z. J. Farrell, C. Tabor, *Langmuir* **2018**, *34*, 234.

[30] N. Ilyas, A. Cook, C. E. Tabor, *Adv. Mater. Interfaces* **2017**, *4*, 1700141.

[31] S. Catalán-Gómez, A. Redondo-Cubero, F. J. Palomares, F. Nucciarelli, J. L. Pau, *Nanotechnology* **2017**, *28*, 405705.

[32] T. R. Lear, S.-H. Hyun, J. W. Boley, E. L. White, D. H. Thompson, R. K. Kramer, *Extreme Mech. Lett.* **2017**, *13*, 126.

[33] S. S. Hafiz, D. Labadini, R. Riddell, E. P. Wolff, M. Xavierselvan, P. K. Huttunen, S. Mallidi, M. Foster, *Part. Part. Syst. Charact.* **2020**, *37*, 1900469.

[34] D. Drabik, M. Gavutis, R. N. Valiokas, A. R. Ulčinas, *Langmuir* **2020**, *36*, 13251.

[35] E. Glynos, V. Koutsos, W. N. McDicken, C. M. Moran, S. D. Pye, J. A. Ross, V. Sboros, *Langmuir* **2009**, *25*, 7514.

[36] J. D. Berry, S. Mettu, R. R. Dagastine, *Soft Matter* **2017**, *13*, 1943.

[37] C. C. Surdu-Bob, S. O. Saied, J. L. Sullivan, *Appl. Surf. Sci.* **2001**, *183*, 126.

[38] M. Grabau, H.-P. Steinrück, C. Papp, *Surf. Sci.* **2018**, *677*, 254.

[39] C. J. Powell, A. Jablonski, I. S. Tilinin, S. Tanuma, D. R. Penn, *J. Electron Spectrosc. Relat. Phenom.* **1999**, *98–99*, 1.

[40] A. K. Battu, C. V. Ramana, *Adv. Eng. Mater.* **2018**, *20*, 1701033.

[41] M. P. Neubauer, M. Poehlmann, A. Fery, *Adv. Colloid Interface Sci.* **2014**, *207*, 65.

[42] J. L. Hutter, J. Bechhoefer, *Rev. Sci. Instrum.* **1993**, *64*, 1868.

[43] J. E. Sader, J. W. M. Chon, P. Mulvaney, *Rev. Sci. Instrum.* **1999**, *70*, 3967.